electron-induced growth, although the decomposition occurs locally, the reaction products are mobile on the surface. Here we believe an analogy can be drawn between the deposition of nanoscale filaments and thin film nucleation and growth theory. We observe that metallic (>50% iron) deposits do not grow until the decomposition rate is sufficiently rapid that critically sized clusters form under the tip. This rate, in the present experiments, is limited by the adsorption of precursors on the surface and hence the pressure. We find that below $\sim 10^{-6}$ torr filaments do not form and the reaction products are dispersed on the surface like the background in Fig. 2. As we have illustrated, increasing the pressure reduces the spatial extent of the background and allows the formation of iron-rich deposits. The minimum diameter of metallic clusters is ~ 10 nm. We expect that smaller iron clusters could be formed if the mobility of adatoms on the surface were reduced by, for example, cooling the substrate.

In contrast to this behavior, in the case of field-induced reactions, there is little or no diffusion of material. The reaction occurs in the high-field regions of the STM junction, and the products are apparently immobilized. The resulting structures are carbonaceous filaments with a small percentage of iron.

In conclusion, the ability to fabricate and position magnets on a nanometer scale offers unique scientific and technological opportunities. For example, increasing the storage capacity of magnetic media requires, among other important practical considerations, reducing the size of magnetized domains. At a certain dimension even in the absence of thermal activation, macroscopic quantum tunneling of the magnetization is predicted to occur and to present a fundamental quantum limit to magnetic storage (19). Moreover, the combination of nanomagnets with present semiconductor technology may lead to new classes of magnetically active devices that rely on the interplay between magnetic and electronic degrees of freedom in confined geometries. STM structures will permit studies of the ramifications of such magnetic miniaturization.

REFERENCES AND NOTES

1. For a recent review, see, for example, C. F. Quate, in *Highlights of the 80's and Prospects for the 90's in Condensed Matter Physics*, L. Esaki, Ed. (Plenum, New York, 1991), pp. 573–630.
2. D. M. Eigler and E. K. Schweizer, *Nature* **344**, 524 (1990).
3. L. J. Whitman, J. A. Stroscio, R. A. Dragoset, R. J. Celotta, *Science* **251**, 1206 (1991).
4. I.-W. Lyo and P. Avouris, *ibid.* **253**, 173 (1991).
5. For a recent review, see P. A. Dowben, J. T. Spencer, G. T. Stauf, *Mater. Sci. Eng. B* **2**, 297 (1989).
6. R. M. Silver, E. E. Ehrichs, A. L. de Lozanne, *Appl. Phys. Lett.* **51**, 247 (1987).
7. E. E. Ehrichs, R. M. Silver, A. L. de Lozanne, *J. Vac. Sci. Technol. A* **6**, 540 (1988).
8. E. E. Ehrichs, W. F. Smith, A. L. de Lozanne, *Ultramicroscopy* **42–44B**, 1438 (1991).
9. M. A. McCord, D. P. Kern, T. H. P. Chang, *J. Vac. Sci. Technol. B* **6**, 1877 (1988).
10. M. A. McCord and D. D. Awschalom, *Appl. Phys. Lett.* **57**, 2153 (1990).
11. Somewhat larger scale deposits produced by high-voltage electron beam decomposition of metal organics have been characterized by TEM and AES. See, for example, K. L. Lee and M. Hatzakis [*J. Vac. Sci. Technol. B* **7**, 1941 (1989)] and S. Matsui and T. Ichihashi [*Appl. Phys. Lett.* **53**, 843 (1988)].
12. Burleigh Instruments–ARIS 5100 UHV-STM.
13. An optical microscope provides a view of the tip-sample junction, and a coarse *x-y* sample translation stage allows positioning of the tip with respect to registration marks on the substrate. Positional control is necessary for locating deposits for analysis in an SEM and AES system.
14. The wafers were chemically cleaned and hydrogen terminated by dipping in dilute HF (5:1 H_2O:HF) just before being put in vacuum. They were then flashed (5 to 10 s) in situ to 700°C to desorb the hydrogen and leave a clean silicon surface. The depositions were performed at room temperature with both electrochemically etched tungsten wire and microfabricated silicon tips (Nanoprobe, Aidlingen, Germany, noncontact atomic force microscopy all-silicon integrated cantilevers).
15. Iron pentacarbonyl is autocatalytic, decomposing in the presence of iron. See, for example, (*18*).
16. D. D. Awschalom, A. D. Kent, S. von Molnár, in preparation.
17. H. B. Linden, E. Hilt, H. D. Beckey, *J. Phys. E* **11**, 1033 (1978).
18. D. F. Shriver and K. H. Whitmore, in *Comprehensive Organometallic Chemistry*, G. Wilkinson, F. Stone, E. Abel, Eds. (Pergamon, New York, 1982), vol. 4, pp. 243–319.
19. D. D. Awschalom, D. P. DiVincenzo, J. F. Smyth, *Science* **258**, 414 (1992).
20. We thank D. Beach, M. McCord, M. Yu, and D. DiVincenzo for helpful advice and discussions and B. Schad for the AES measurements. This work was supported in part by the Air Force Office of Scientific Research grant F49620-93-1-0117.

Uncertainties in Carbon Dioxide Radiative Forcing in Atmospheric General Circulation Models

R. D. Cess, M.-H. Zhang, G. L. Potter, H. W. Barker, R. A. Colman, D. A. Dazlich, A. D. Del Genio, M. Esch, J. R. Fraser, V. Galin, W. L. Gates, J. J. Hack, W. J. Ingram, J. T. Kiehl, A. A. Lacis, H. Le Treut, Z.-X. Li, X.-Z. Liang, J.-F. Mahfouf, B. J. McAvaney, V. P. Meleshko, J.-J. Morcrette, D. A. Randall, E. Roeckner, J.-F. Royer, A. P. Sokolov, P. V. Sporyshev, K. E. Taylor, W.-C. Wang, R. T. Wetherald

Global warming, caused by an increase in the concentrations of greenhouse gases, is the direct result of greenhouse gas–induced radiative forcing. When a doubling of atmospheric carbon dioxide is considered, this forcing differed substantially among 15 atmospheric general circulation models. Although there are several potential causes, the largest contributor was the carbon dioxide radiation parameterizations of the models.

The most comprehensive way to estimate climate change caused by increasing concentrations of greenhouse gases is to use three-dimensional general circulation models (GCMs). But even for the most straightforward climate-change simulation, a change in equilibrium climate that results from a doubling of atmospheric CO_2, there is a roughly threefold variation in the predicted increase in global mean surface temperature (1, 2) (Fig. 1). Global climate change caused by a CO_2 doubling may be conceptually interpreted as a two-stage process: forcing and response. The forcing is the direct radiative perturbation caused by the CO_2 increase, whereas the response is the climate change associated with restoring the global-mean radiation balance. Climate feedback mechanisms that govern the response differ substantially among GCMs (3–7), but it is not known to what extent differences in Fig. 1 are attributable to variations in forcing among models. In an earlier comparison (8), significant differences were found in CO_2 radiative forcing from radiation codes used in several GCMs.

Potential forcing differences attributable to other facets of the GCMs were not, however, addressed. These included:

1) Forcing is dependent on lapse rate, which is the decrease of atmospheric temperature with height. Because CO_2 forcing is a change in the greenhouse effect, it could be affected by differences in lapse rate among models (9).

2) The forcing is substantially reduced through radiative overlap of the CO_2 absorption bands by the absorption of water vapor (8), so differences in atmospheric water vapor distributions among models could likewise affect CO_2 forcing, as well as differences in the parameterization of radiative overlap in the radiation codes.

3) Clouds also reduce the forcing (10), so the substantial differences among different GCMs' cloud fields (6) could cause forcing differences.

In this study we specifically address these

Fig. 1. Summary of the increase in global mean equilibrium surface temperature caused by a doubling of atmospheric CO_2 concentrations. These results are from simulations with atmospheric GCMs with a seasonal cycle, a mixed layer ocean, and interactive clouds. Multiple simulations were performed for several models in the context of sensitivity studies related to specific processes. Changes in cloud parameterizations for the United Kingdom Meteorological Office GCM produced the greatest differences (3, 4). This figure is taken from table 3.2(a) of (1) and table B2 of (2), and the model acronyms are those used in these two references. The coefficient of variation (CV) is the standard deviation divided by the mean.
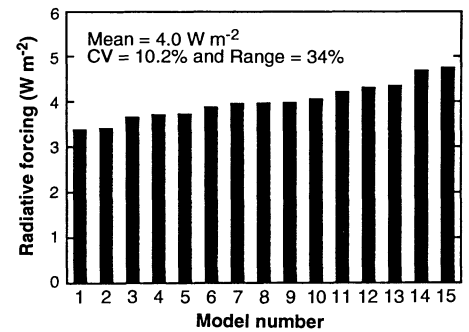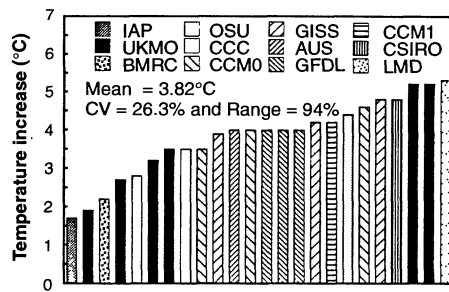

Fig. 2. Summary of global mean CO_2 radiative forcing for the 15 GCMs used in the current study.

issues so as to better understand the differences shown in Fig. 1.

We can define CO_2 forcing as the reduction in net upward radiative flux at the tropopause (top of the troposphere) caused by the CO_2 increase, with all other climate parameters held fixed. It is thus the direct radiative heating of the surface-troposphere system, which acts as a single thermodynamic system because the surface and troposphere are convectively coupled (10). We have adopted a global mean tropopause at 200 mbar. The CO_2 mixing ratio was increased from 330 to 660 parts

R. D. Cess and M.-H. Zhang, Institute for Terrestrial and Planetary Atmospheres, Marine Sciences Research Center, State University of New York, Stony Brook, NY 11794.
G. L. Potter, W. L. Gates, K. E. Taylor, Lawrence Livermore National Laboratory, Livermore, CA 94550.
H. W. Barker, Canadian Climate Centre, Downsview, Ontario, Canada M3H 5T4.
R. A. Colman, J. R. Fraser, B. J. McAvaney, Bureau of Meteorology Research Centre, G.P.O. Box 1298K, Melbourne, 3001 Victoria, Australia.
D. A. Dazlich and D. A. Randall, Colorado State University, Fort Collins, CO 80523.
A. D. Del Genio and A. A. Lacis, National Aeronautics and Space Administration Goddard Institute for Space Studies, 2880 Broadway, New York, NY 10025.
M. Esch and E. Roeckner, Max Planck Institute for Meteorology, Bundesstrasse 55, D2000, Hamburg 13, Germany.
V. Galin, Department of Numerical Mathematics, Russian Academy of Sciences, 32A Leninsky Prospect, Moscow, 117334, Russia.
J. J. Hack and J. T. Kiehl, National Center for Atmospheric Research, Boulder, CO 80307.
W. J. Ingram, Hadley Centre for Climate Prediction and Research, Meteorological Office, London Road, Bracknell, Berkshire RG12 2SY, United Kingdom.
H. Le Treut and Z.-X. Li, Laboratoire de Météorologie Dynamique, 24 Rue Lhomond, 75231 Paris Cedex 05, France.
X.-Z. Liang and W.-C. Wang, Atmospheric Sciences Research Center, State University of New York, Albany, NY 12205.
J.-F. Mahfouf and J.-F. Royer, Direction de la Météorologie Nationale, Centre National de Recherches Météorologiques, 42 Avenue Coriolis, 31057 Toulouse Cedex, France.
V. P. Meleshko, A. P. Sokolov, P. V. Sporyshev, Voeikov Main Geophysical Observatory, 7 Karbisheva Street, 194018 St. Petersburg, Russia.
J.-J. Morcrette, European Centre for Medium-Range Weather Forecasts, Reading, Berkshire RG29AX, United Kingdom.
R. T. Wetherald, Princeton University, National Oceanic and Atmospheric Administration, Geophysical Fluid Dynamics Laboratory, Post Office Box 308, Princeton, NJ 08540.

per million (ppm) by volume, and we evaluated the forcing by performing a second radiation computation, for 660 ppm of CO_2, during the control climate (330 ppm of CO_2) averaging period. The 660-ppm radiation calculation was performed at the same times as the 330-ppm calculation, with the forcing comprising the 200-mbar radiative flux difference between the two calculations (11, 12). To evaluate the impact of clouds, clear-sky forcing was evaluated by Method II (13), by which clear-sky fluxes are computed at each grid point.

The GCM results (identified by number, Table 1) are from two perpetual July runs similar to those used earlier (5, 6). In the first, the sea-surface temperature was set 2°C below the typical 15 July values and in the second 2°C above; we report only the cold run results. The results show that the range and coefficient of variation (CV) of

net forcing, the sum of the LW (longwave; terrestrial thermal radiation) and SW (shortwave; solar radiation) contributions, are substantial (Fig. 2) and could account for more than one-third of the differences among the models (Fig. 1), although Figs. 1 and 2 refer to different sets of GCMs.

Although near-infrared bands of CO_2 absorb SW radiation and thus heat the atmospheric column, this heating occurs mostly in the stratosphere; thus, less SW radiation reaches the tropopause, and the SW forcing is negative. On average, this reduced the forcing by 4.7%, whereas, if the models that do not include SW forcing were deleted (models 9, 11, and 15), the reduction would be 6.0%. Because of this small magnitude, SW forcing is a minor contributor to model-to-model differences in net forcing (Table 2).

Table 1. List of GCMs used in the present study.

Model	Investigator
1. European Centre for Medium-Range Weather Forecasts (ECMWF)	Potter, Morcrette, Gates
2. Laboratoire de Météorologie Dynamique (LMD)	Le Treut and Li
3. National Center for Atmospheric Research (NCAR) Community Climate Model, Version 2 (CCM2)	Zhang, Cess, Kiehl, Hack
4. ECMWF, Max Planck Institute for Meteorology, Hamburg (ECHAM)	Roeckner and Esch
5. Main Geophysical Observatory (MGO)	Meleshko, Sokolov, Sporyshev
6. State University of New York; Institute for Atmospheric Physics, Beijing (SUNY/IAP)	Liang and Wang
7. Canadian Climate Centre (CCC)	Barker
8. United Kingdom Meteorological Office (UKMO)	Ingram
9. NCAR Community Climate Model, Version 1; Lawrence Livermore National Laboratory (CCM/LLNL)	Taylor
10. Bureau of Meteorology Research Centre (BMRC)	McAvaney, Fraser, Colman
11. Colorado State University (CSU)	Randall and Dazlich
12. NASA Goddard Institute for Space Studies (GISS)	Lacis and Del Genio
13. Geophysical Fluid Dynamics Laboratory (GFDL)	Wetherald
14. Centre National de Recherches Météorologiques (CNRM)	Mahfouf and Royer
15. Department of Numerical Mathematics of the Russian Academy of Sciences (DNM)	Galin

Radiative overlap by water vapor is often regarded as a major source of uncertainty (8). To isolate differences caused by this factor, we modified the radiation codes for all GCMs except model 14 so as to remove overlap. The LW clear (with clouds removed) forcings with and without overlap are correlated (Fig. 3A) and show that variations about the linear fit are the actual contributions by water vapor overlap to forcing differences; the standard deviation (SD) of this residual is only 0.12 W m^{-2}. This small SD includes model-to-model differences in both humidity profiles and the way overlap is parameterized in the radiation codes.

To further isolate differences caused by model-to-model variations in humidity profiles and lapse rates, we inserted humidity profiles and lapse rates for a standard mid-latitude summer atmosphere (8) into column (one-dimensional) versions of the GCM radiation codes. As shown in Fig. 3B, these were not significant sources of differences because the column model calculations adopt a single humidity profile and lapse rate. We confirmed this result by inserting global mean humidity profiles and lapse rates for the GCMs into the CCM2 column radiation code. The LW clear forcings computed in this manner were in remarkable agreement; SD = 0.03 W m^{-2} without overlap and 0.06 W m^{-2} with overlap. The implied invariance with vertical resolution is consistent with the results of a related sensitivity study in which vertical resolution was varied in the CCM2 column radiation code while the humidity profile and lapse rate were kept fixed. Although inclusion of clouds reduced the LW forcing by an average 14% and there are substantial differences among the GCMs' cloud fields (6), clouds were not a major cause of LW forcing differences (Fig. 3C).

The largest single cause of forcing differences was model-to-model differences in the LW radiation codes for CO_2 (Table 2). Earlier GCM comparisons (5–7) considered climate change feedback mechanisms for which there are no standards for comparison. For CO_2 forcing, however, line-by-line (LBL) calculations of LW clear forcing are available as

standards of comparison (8). Deviations of the GCM column model forcings from the LBL results, both with and without water-vapor overlap, are large for many models (Fig. 4A), particularly those that predict low forcings. Although results for model 14 (which was not included in Fig. 3A because "without water vapor overlap" GCM forcing was not available) agreed well with the LBL results when water vapor overlap was included, there was substantial disagreement in the forcing without water vapor overlap. Here, overly strong overlap compensated for a positive forcing bias produced by this model's CO_2 radiation code.

The tendency for models to underestimate LW clear forcing (Fig. 4A) is partly a result of the neglect of certain CO_2 absorption bands. This gas has a dominant 15-μm band complex, but also has absorption bands at 10.4, 9.4, and 4.3 μm. None of the models incorporated the 4.3-μm band; the 10.4- and 9.4-μm bands are included in models 1, 2, 5, 7, 11, and 13 but not in the other models. A fairer test (although not a test of reality) of the radiation codes is to delete those bands in the LBL calculation that are not included in the respective GCM radiation codes. This did reduce the tendency of the models to under-
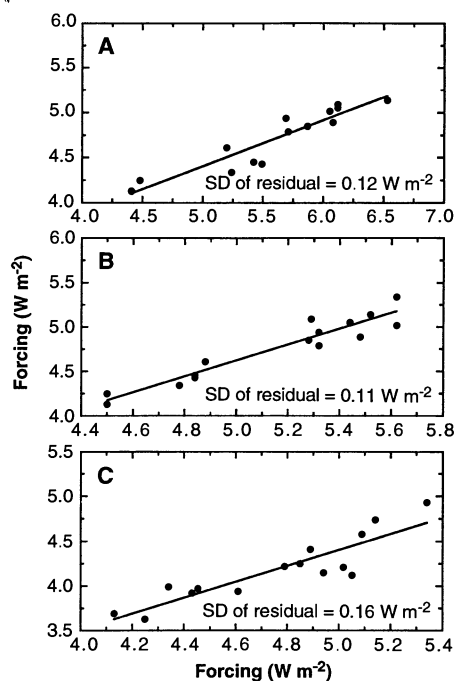
estimate the forcing (Fig. 4B). Models 1 and 2 share the same LW radiation code.

The models in Fig. 1 produced an average global warming close to 4°C, whereas the models in our study produced an average CO_2 forcing of 4.0 W m^{-2}, so this amounts to an average climate sensitivity of 1°C of warming for each 1 W m^{-2} of forcing. Now imagine 15 GCMs, all with the same climate sensitivity, a 1°C warming per 1 W m^{-2} forcing, but CO_2 forcing varying like the 15 GCMs in this study. They would give global warming projections ranging from 3.4° to 4.7°C just because of their forcing differences (Fig. 2). This range is substantial and is nearly half of the often quoted range of uncertainty of 1.5° to 4.5°C (1, 14), which has been based on feedback uncertainties assuming no differences in the forcing.

Ideally one would like to use these results to isolate differences in Fig. 1 that are attributable to forcing differences. But the perpetual July forcings may not be representative of annual mean forcings. Nor is the present set of GCMs the same as in Fig. 1, for which the forcings would have to refer to the same averaging period as used for the doubled CO_2 climate simulations. The inclusion of forcing values would be reasonably straightforward to accomplish when the simulations are performed (12), and future studies should provide CO_2 forcing values as a routine diagnostic.

Table 2. Summary of standard deviation (SD) and range for individual processes contributing to differences in CO_2 radiative forcing.

Process	SD (W m^{-2})	Range (W m^{-2})
CO_2 SW radiation*	0.08	0.32
Water-vapor overlap†	0.12	0.41
Temperature and humidity profile differences†	0.11	0.37
Clouds (LW)†	0.16	0.58
CO_2 LW radiation	0.62	2.12

*Refers only to those models that include SW forcing. †Computed as the residual (see Fig. 3).

Fig. 3. (A) Scatter plot of LW clear (clear sky) radiative forcing, as generated by the GCMs, with and without overlap of the CO_2 absorption bands by water vapor absorption. (B) Scatter plot of LW clear forcing as generated by the GCMs versus those generated by their respective column models using the standard mid-latitude summer atmosphere. (C) Scatter plot of LW cloudy (all sky) forcing versus LW clear forcing as generated by the GCMs. In (A) through (C) the solid line represents a linear root-mean-square fit.
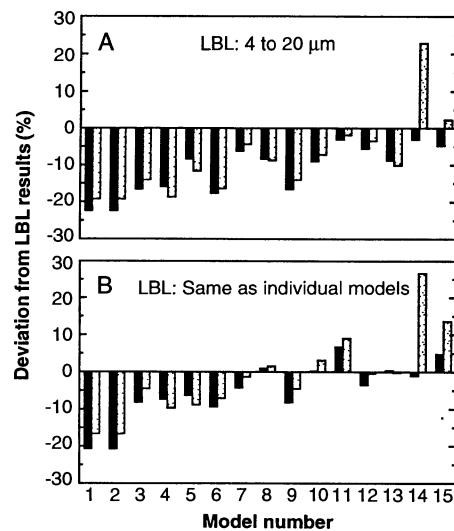

Fig. 4. (A) Percent deviation of the GCM LW column model tropopause forcings from reference LBL results for mid-latitude summer temperature and humidity profiles (8). The LBL values are 5.80 W m^{-2} with water vapor overlap (solid bars) and 6.90 W m^{-2} without (stippled bars). (B) The same as (A) but with CO_2 bands removed in the LBL calculation so as to represent those included in the GCMs (see text). With the 4.3-μm band removed, the LBL values are 5.68 W m^{-2} with water vapor overlap and 6.69 W m^{-2} without. With additional removal of the 9.4- and 10.4-μm bands, these respective values are 5.27 and 6.21 W m^{-2}.

Because the global mean temperature increase is linearly proportional to the CO_2 forcing, a figure similar to Fig. 1 but showing the ratio of the temperature increase to the CO_2 forcing would be far more informative because this normalized temperature increase would remove forcing differences and so isolate differences caused by feedback processes (12).

REFERENCES AND NOTES

1. J. T. Houghton, G. J. Jenkins, J. J. Ephraums, Eds., Climate Change: The IPCC [Intergovernmental Panel on Climate Change] Scientific Assessment (Cambridge Univ. Press, Cambridge, 1990).

2. J. T. Houghton, B. A. Callander, S. K. Varney, Eds., Climate Change 1992: The Supplementary Report to the IPCC Scientific Assessment (Cambridge Univ. Press, Cambridge, 1992).
3. J. F. B. Mitchell et al., Nature 341, 132 (1989).
4. C. A. Senior and J. F. B. Mitchell, J. Clim. 6, 393 (1993).
5. R. D. Cess et al., Science 245, 513 (1989).
6. R. D. Cess et al., J. Geophys. Res. 95, 16601 (1990).
7. R. D. Cess et al., Science 253, 888 (1991).
8. R. G. Ellingson et al., J. Geophys. Res. 96, 8929 (1991).
9. A. Raval and V. Ramanathan, Nature 342, 758 (1989).
10. V. Ramanathan et al., J. Geophys. Res. 84, 4949 (1979).
11. C. Schmitt and D. A. Randall, ibid. 96, 9159 (1991).

12. R. D. Cess and G. L. Potter, ibid. 93, 8305 (1988).
13. _____, Tellus Ser. A 39, 460 (1987).
14. Carbon Dioxide and Climate: A Scientific Assessment (National Academy of Sciences Press, Washington, DC, 1979).
15. This study was performed under the auspices of the Environmental Sciences Division of the U.S. Department of Energy. Additional support was provided by the National Aeronautics and Space Administration, the National Science Foundation, the Bundesminister für Forschung and Technologie (Germany), the French Climate Program, and the Commission of European Communities. We thank M. D. Schwartzkopf for supplying the line-by-line results.

28 June 1993, accepted 13 September 1993

Photocrosslinking of 5-Iodouracil–Substituted RNA and DNA to Proteins

Michael C. Willis, Brian J. Hicke, Olke C. Uhlenbeck, Thomas R. Cech, Tad H. Koch*

5-Iodouracil–substituted RNA and DNA were crosslinked regiospecifically to associated proteins in yields of 70 to 94% of bound nucleic acid. Irradiation of the iodouracil chromophore with monochromatic, long-wavelength ultraviolet radiation (325 nanometers) eliminates excitation of other nucleic acid and protein chromophores. The combination of high crosslinking yields, excellent specificity, and elimination of photodamage to other chromophores represents an important advance toward the precise identification of contacts in nucleoprotein complexes.

During the past two decades 5-bromodeoxyuridine (BrdU) has been incorporated into DNA to enhance photosensitivity (1). Photoreactions include formation of single- and double-strand breaks, alkali labile bonds, and crosslinks to associated proteins. Of particular interest has been photocrosslinking to associated proteins to establish point contacts as a method for partially defining the structure of nucleoprotein complexes. Low-level 5-bromodeoxyuridine–DNA (BrdU-DNA) photocrosslinking to associated proteins has been reported (2–4), and in two cases point contacts have been established (3, 4). 5-Bromouridine–RNA (BrU-RNA) photocrosslinking to associated proteins has also been reported (5, 6), including R17 bacteriophage coat protein to singly BrU-substituted hairpin RNA 1 (Fig. 1) (6).

Creation of a photoreactive nucleic acid chromophore by replacement of the methyl group of thymine with a bromine is attractive because the van der Waals radius of bromine (1.95 Å) is similar to the size of a methyl group (2.0 Å). The van der Waals radius of iodine is 2.15 Å, only 8% larger than the methyl group. A single substitution of IdU for T also does not appreciably disturb the protein-DNA complex studied here (Fig. 1). Even the single BrU or IU for U substitution in the binding site for bacteriophage R17 coat protein (RNA 1 or RNA 2, respectively) does not interfere with binding. In fact, the bacteriophage R17 coat protein binds RNA 2 as well as RNA 1 and better than its uridine equivalent (RNA 3).

RNAs 1 and 2 both undergo photocrosslinking to the R17 coat protein; yields as a function of time of irradiation at 308 nm with a XeCl excimer laser are compared in Fig. 2. Crosslinking of the IU–RNA 2–R17 coat protein complex leveled off at 80% in less than 5 min of irradiation, whereas the corresponding BrU–RNA 1–R17 coat protein crosslinking leveled off at 40% after 15 min of irradiation. The two crosslinked nucleoprotein complexes showed identical electrophoretic migration in both SDS- and urea-denaturing polyacrylamide gels (7). Crosslinking to Tyr^{85} of the coat protein was established with BrU–RNA 1 (8). The lower crosslinking yield with BrU-RNA was a consequence of protein damage (6). Crosslinking as a func-

tion of photons absorbed indicated that the quantum yield for crosslinking of BrU–RNA 1 is actually about twice that of IU–RNA 2 (0.014 as compared with 0.006, respectively) (9). In spite of the lower quantum yield with IU substitution, a higher crosslinking yield was obtained as a result of the sevenfold higher absorption probability of the IU chromophore at 308 nm. Hence, a high level of photocrosslinking was achieved before protein damage. Placement of IU at other positions in the hairpin, as described previously for BrU substitution (6), did not yield appreciable photocrosslinks or RNA damage.

Having established the superiority of the iodouracil chromophore upon excitation at 308 nm, we tried excitation at a longer wavelength where other nucleoprotein chromophores do not absorb. The photocrosslinking yield of IU–RNA 2 to the R17 coat protein as a function of irradiation time with monochromatic, 325-nm light from a helium cadmium (HeCd) laser is shown in Fig. 3 (10).

	X	K_d (nM)
1	BrU	3.4
2	IU	5.2
3	U	15.7

	X
4	T
5	IdU

Fig. 1. Structures of the R17 bacteriophage RNA hairpins 1, 2, and 3 (14) and the Oxytricha nova telomeric DNA oligonucleotides 4 and 5 (15) (N_{24} represents 24 nucleotides of nontelomeric DNA). The dissociation constants of the RNA-protein complexes were determined with a nitrocellulose filter retention assay (16). For each experiment the data points were fit to a noncooperative binding curve and the dissociation constant (K_d) calculated. The telomeres of the ciliated protozoan O. nova have 3′ single-stranded $(T_4G_4)_2$ extensions bound by a heterodimeric protein.

M. C. Willis, O. C. Uhlenbeck, T. H. Koch, Department of Chemistry and Biochemistry, University of Colorado, Boulder, CO 80309.
B. J. Hicke, Department of Molecular, Cellular, and Developmental Biology, Howard Hughes Medical Institute, University of Colorado, Boulder, CO 80309.
T. R. Cech, Department of Chemistry and Biochemistry and Department of Molecular, Cellular, and Developmental Biology, Howard Hughes Medical Institute, University of Colorado, Boulder, CO 80309.

*To whom correspondence should be addressed.